Dalton Transactions

ROYAL SOCIETY OF CHEMISTRY

PAPER

View Article Online
View Journal | View Issue

Cite this: *Dalton Trans.*, 2026, **55**, 5519

Synthesis, structural characterization and rigidity dependent dual phosphorescence behavior of high-energy phosphorescent zinc(II) cyclic (alkyl)(amino)carbene complexes

Mousree Mitra,[a] Ondřej Mrózek,[a] Andrey Belyaev,[a] Lars Janiak,[a] Christel M. Marian[b] and Andreas Steffen*[a]

The study explores the synthesis, structural characterization, and photophysical properties of cyclic (alkyl)(amino)carbene (cAAC) zinc(II) complexes, focusing on their unique rigidity-dependent dual phosphorescence behavior. Starting from previously reported dimeric $[Zn_2X_2(\mu\text{-}X)_2(cAAC)_2]$ (X = Cl, Br), halide abstraction with Et_3Si^+ gives dicationic tetramers with an adamantyl-like Zn_4X_6 core, while the reaction with Na(acac) (acac = acetylacetonate) or KCz (Cz = carbazolate) leads to ligand exchange and isolation of [ZnCl(acac)(cAAC)] (**11**) and [ZnCl(Cz)(THF)(cAAC)] (**12**), respectively. While **12** displays orange phosphorescence from ^{3}LLCT (LLCT = ligand-to-ligand charge transfer) states both at room temperature and at 77 K, complex **11** and the tetrameric compounds exhibit excitation wavelength-dependent unusual high-energy UV-blue phosphorescence and green-yellow luminescence. The experimental data suggest that high-energy excitation leads to emission primarily from high-energy states due to strong Franck–Condon overlaps, while low-energy excitation enables direct triplet state population and geometry-driven transitions. This behavior, influenced by the molecular rigidity, appears to be the result of an equilibrium between different excited states and emphasizes the impact of the molecular structure on the emission profiles.

Received 22nd January 2026,
Accepted 4th March 2026

DOI: 10.1039/d6dt00177g

rsc.li/dalton

Introduction

Cyclic (alkyl)(amino)carbene (cAAC) complexes of transition metals (TM) are a highly interesting class of compounds with diverse applications in (photo)catalysis,[1–9] organic synthesis,[1,3] and the development of photoluminescent and photoactive materials,[10–12] which can be traced back to the unique electronic and steric properties of the carbene. Modifying the substituents on the α-carbon of the cAAC ligand provides steric control, enabling the formation of stable, unusual low-coordinate metal complexes, such as cationic [Pd(allyl)(^{Menth}cAAC)]BF_4 (Menth = menthyl),[13] [Au(^{Ad}cAAC)(tol)][$B(C_6F_5)_4$][14] (Ad = adamantyl, tol = toluene) or [Zn(bdt′)(^{Menth}cAAC)] (bdt′ = benzene-1,2-dithiolate and its derivatives).[15] In addition to their steric effects, cAAC ligands exhibit significantly higher π-accepting properties than traditional N-heterocyclic carbenes (NHCs) of imidazolylidene and imidazoline-2-ylidene types, a critical component for stabilization of transition metals in unusual low oxidation states, as observed in Au^0, Ni^0, Mn^0, and Zn^0 complexes.[1,4–9]

Electrophilic cAAC ligands can also serve as highly efficient excited state π electron density acceptors, facilitating the generation of metal-to-ligand charge transfer (MLCT) or ligand-to-ligand charge transfer (LLCT) excited states that are important to realize visible light absorption and luminescence in TM complexes. In the last decade, d^{10} coinage metal (Cu/Ag/Au) cAAC complexes have been studied extensively regarding their photophysical and chemical properties.[12,16] The great potential and important influence of the carbene ligand on the excited state behaviour is nicely exemplified by analysis of linear [Cu(^{Me}cAAC)$_2$]PF_6 reported by Gernert *et al.*, which exhibits intense blue phosphorescence $T_1 \rightarrow S_0$ both in the solid state and in PMMA films with high radiative rate constants (k_r = 2.3–9.4 × 10^4 s^{-1}), making it one of the fastest phosphorescent Cu^I emitters known to date.[10] In contrast, structurally related [Cu(IDipp)$_2$]PF_6 bearing NHC ligands is barely emissive and lacks a visible MLCT band in the UV-Vis absorption spectrum.[10] This stark difference in luminescence behaviour can be attributed to the lower LUMO energy of the cAAC ligand compared to IDipp, leading to an enhanced MLCT contribution in the T_1 state, facilitating strong spin–orbit coupling

[a]*Department of Chemistry and Chemical Biology, TU Dortmund University, Otto-Hahn-Str. 6, 44227 Dortmund, Germany. E-mail: andreas.steffen@tu-dortmund.de*
[b]*Institute of Theoretical and Computational Chemistry, Heinrich Heine University Düsseldorf, 40225 Düsseldorf, Germany*

(SOC) with singlet excited states to enable efficient phosphorescence. Subsequent studies have shown that construction of D–Cu^{I}–A (D = donor, A = acceptor) motifs greatly extends the space of photophysical properties. For example, carbene–metal–amides (CMA) can achieve outstanding k_r of up to 10^6 s^{-1} for blue to orange emission involving triplet states.[12,17] In these systems, the emission mechanism shifts from phosphorescence to thermally activated delayed fluorescence (TADF) due to a very small energy gap ΔE_{S1-T1} between singlet and triplet excited states of LLCT character, which allows thermal repopulation of the fluorescent S_1 state by reverse intersystem-crossing (rISC) at room temperature.[18,19] Consequently, CMAs have successfully been incorporated into organic light-emitting diodes (OLEDs), demonstrating efficient electroluminescence and underscoring their potential for optoelectronic applications.

Despite the similar d^{10} electronic configuration, the number of thoroughly investigated luminescent Zn^{II} complexes is relatively small, with the majority being purely fluorescent.[20–29] This limitation arises primarily from zinc's high ionization potential $Zn^{II} \rightarrow Zn^{III}$, which prevents the formation of metal-to-ligand charge transfer (MLCT) states—essential for facilitating efficient spin–orbit coupling (SOC) required for formal spin-forbidden processes (r)ISC or phosphorescence. As a result, when designing zinc-based photonic materials that involve triplet excitons, key strategies focus on promoting $^{1/3}$LLCT and intraligand ($^{1/3}$IL) CT excited states with small energy gaps between the singlet and triplet excited states to reduce the significance of SOC and enable TADF.[18,19,30–33]

One notable approach involves the work by Adachi *et al.*,[34] who used phenylbenzoxazole derivatives to achieve a small ΔE_{S1-T1} *via* spatial separation of HOMO and LUMO. These complexes exhibit TADF with good quantum yields of up to 50–60% in mCPB matrices at room temperature, resulting in external quantum efficiencies (EQE) of 19.6% when used as emitters in OLEDs. In the 1980s, Crosby and colleagues studied a series of heteroleptic Zn^{II} complexes of 1,10-phenanthroline and thiophenolate ligands, observing weak phosphorescence from ^{3}LLCT states, and many subsequent works were built on this interpretation.[35–40] However, more recent work by our group, aided by detailed spectroscopic and quantum mechanical calculations, revealed that these complexes show TADF with high radiative rate constant (k_r) up to 3.5×10^5 s^{-1} at room temperature, but non-radiative decay is more facile and thus the compounds are very inefficient emitters.[41]

Phosphorescence remains an even rarer phenomenon for zinc(II)-based emitters with the exception of porphyrins.[23,24] However, recent work has demonstrated a series of low-coordinate Zn^{II} complexes featuring sterically demanding ITr ligands to achieve long-lived phosphorescence from ^{3}LLCT or ^{3}LC state.[42] In 2022, we investigated the photophysical and photochemical properties of a series of dimeric and monomeric Zn^{II} halide complexes bearing cAAC ligands, which show rare ultra-long-lived luminescence originating from ^{3}XLCT/LE_{cAAC} states.[43] However, these Zn^{II} cAAC complexes were found to be highly photolabile, most likely due to asymmetric distortion of the carbene ligand and halide dissociation among other unidentified processes. Despite this photo-instability, the study underscores the potential of cAAC ligands for expanding the photophysical properties of zinc(II) complexes.

To address the limitations of photostability and explore the potential for more stable photoluminescent Zn^{II} cAAC compounds, we investigated the use of halide dimers as precursors for ligand exchange.[15,44] This approach allowed access to a variety of coordination geometries and ligand combinations, which modulated the photophysical properties of the resulting zinc(II) carbene complexes. One such strategy involved synthesizing a new class of Zn^{II} TADF compounds by incorporating dithiophenolate ligands as electron-donating moieties and exploring different cAAC substitutions. Remarkably, these complexes demonstrated radiative rate constants (k_r) up to 1.2×10^6 s^{-1} at room temperature—setting a record for Zn^{II}-based emitters, and even competing with well-established rare-metal-based emitters.[15]

In this work, we further explore the structure–property relationships of cAAC-bearing Zn^{II} complexes attempting to access low-coordinated, primarily linear Zn^{II} complexes by halide abstraction. This approach is inspired by the successful design of $[CuL_2](PF_6)$-type compounds, which exhibit triplet excitons and have been instrumental in developing efficient luminescent materials.

Results and discussion

Synthesis and characterisation

We followed the reported synthetic strategy to prepare a series of carbene salts and their corresponding zinc(II) halides **1–5**, which were obtained as crystalline solids in yields of 70–80% (Fig. 1, and SI).[43] Regardless of the *N*-substituent at the cAAC ligand, the chloride complexes consistently formed a dimeric arrangement of type $[Zn_2Cl_2(\mu\text{-}Cl)_2(^{R}cAAC)_2]$ (**1**, **2** and **4**), which was also observed for the bromide derivative **3** bearing ^{Me}cAAC as confirmed by single-crystal X-ray diffraction (SC-XRD). However, upon slow diffusion of *n*-pentane into the reaction

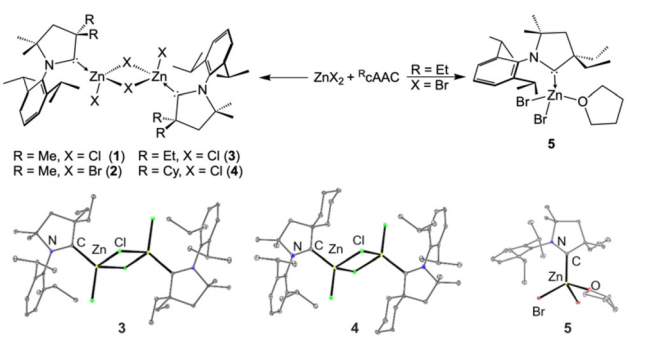

Fig. 1 Top: Synthesis of dimeric $[Zn_2X_2(\mu\text{-}X)_2(cAAC)_2]$ (**1–4**) and of monomeric [ZnBr(THF)(cAAC)] (**5**). Bottom: Molecular structures of **3–5** determined by SC-XRD.

mixture of $ZnBr_2$ with ^{Et}cAAC, the monomeric THF-coordinated bromide complex **5** was isolated (Fig. 1). This monomerization upon solvent coordination is typical for bromide and iodide complexes, attributed to the relatively weaker Zn–X bond strength, as previously observed for $[Zn_2X_2(\mu\text{-}X)_2(^{Me}cAAC)_2]$ (X = Br, I) with CH_3CN coordination.[43] While the $Zn\text{–}C^{carbene}$ bond lengths in compounds **1–4** are very similar (*ca.* 2.05 Å), it is slightly elongated in the monomeric complex **5** to 2.069(1) Å.

We have recently reported the synthesis of tricoordinate Zn^{II} complexes employing the tropylium-substituted carbene ITr, where the aryl substituents induced a low-energy ^{3}LC state with millisecond lifetimes.[42] To enhance the charge transfer (CT) component in these low-coordinate zinc-based emitters, we employed a similar synthetic approach starting from **1–5** bearing more electrophilic cAAC ligands. Curious about the potential access to trigonal and linear complexes, we added one equivalent of the *in situ* prepared strongly halophilic silylium reagent $[(Et_3Si)(toluene)][B(C_6F_5)_4]$[45,46] at room temperature to **1–5** suspended in toluene (Fig. 2). This reaction led to partial halide abstraction and the formation of Zn_4X_6 cluster-type tetramers **6–8** and **10** in 60–80% yield. However, we obtained only a very small amount of compound **9** following halide abstraction, which is likely due to an undesired side reaction between the coordinated THF and the silylium reagent.

Interestingly, the steric demand of the cAAC ligands has a significant impact on product formation as no monomeric or dimeric products were observed. While the reaction proceeded smoothly with chloride and bromide complexes, the corresponding iodide derivatives produced a complex mixture of products with no clear indication of the desired outcome, presumably due to thermodynamic instability.

Colourless single crystals suitable for X-ray diffraction studies were obtained for compounds **6**, **7**, and **9** by gas-phase diffusion of pentane into saturated DCM solutions. Compounds **8** and **10** could only be isolated as microcrystalline powders, regardless of the crystallization conditions. Compounds **6** and **7** are solvated with DCM and crystallized in the monoclinic *C*2/*c* space group, while **9** crystallized in the *Pbca* space group. The X-ray structures of **6**, **7** and **9** reveal a dicationic tetrameric cluster motif and two $[B(C_6F_5)_4]^-$ acting as counter anions (Fig. 3).

The zinc(II) ions exhibit a tetrahedral geometry, with all halides coordinated in a bridging mode. The structural motif resembles an adamantane-like framework, consisting of four zinc ions and six μ^2-bridging halides, with four carbene ligands terminally bound to each metal centre. Such cluster structures have been previously reported for zinc(II) complexes, often involving bridging thiolate or selenolate ligands, and in some cases, methoxy groups with tertiary ammonium as counter cations.[47] The Zn–X bond lengths in compounds **6** (2.28–2.33 Å) and **7** (2.42–2.48 Å) represent the average of the bridging and terminal Zn–X bonds in the dimeric complexes **1** and **2**, while in compound **9**, the Zn–X bond length is 2.42–2.47 Å, similar to that in its monomeric counterpart **5** (2.3694(4)/2.3905(4) Å). In contrast, the $Zn\text{–}C^{carbene}$ bond length in the tetramers (2.030(3)/2.037(2) Å in **6**, 2.030(3)/2.037(2) Å in **7**, 2.046–2.059 Å in **9**) is slightly shorter than in the dimers **1–4** (*ca.* 2.05 Å) or the monomer **5** (2.069(2) Å), indicating increased electron deficiency at the metal center and enhanced σ donation from the carbene to zinc.

Attempts to further characterize compound **9** were not successful due to its low yield and obtained mixtures of various species. As a result, further characterization and photophysical measurements were carried out only for tetramers **6–8** and **10**. The ^{1}H-NMR spectra of compounds **6–8** and **10** in CD_2Cl_2 exhibit one set of sharp signals corresponding to the carbene ligands coordinated to the zinc atom. In the ^{13}C-NMR spectra, the most downfield signal appears at approximately 238 ppm, confirming the coordination of the deprotonated carbene to zinc, even after halide abstraction. The upfield shift of the carbene carbon from 250 ppm (in **1–4**) to 238 ppm further suggests a stronger $Zn\text{–}C^{carbene}$ bond, which is attributed to

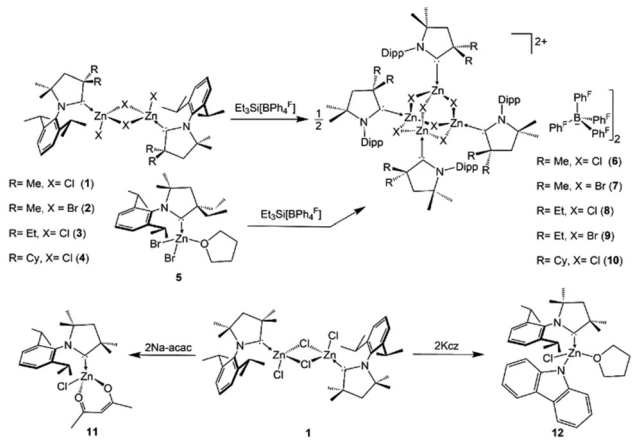

Fig. 2 Synthesis of tetrameric **6–10** by halide abstraction from **1–5**, and ligand exchange reactions of **1** to give [ZnCl(acac)(^{Me}cAAC)] (**11**) and [ZnCl(Cz)(THF)(^{Me}cAAC)] (**12**).

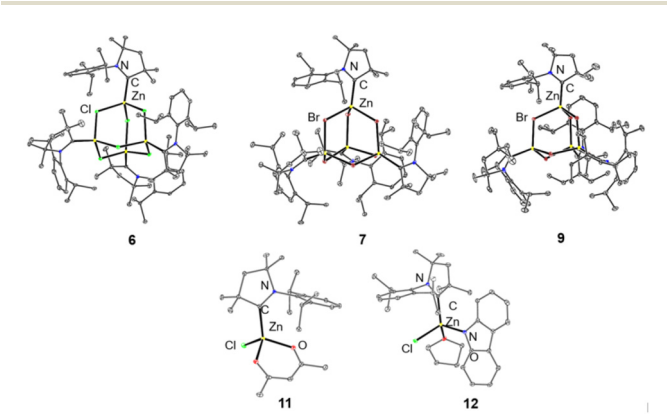

Fig. 3 Molecular structures of **6–12** in the solid state determined by SC-XRD studies. Hydrogen atoms, solvent molecules and counter anions are omitted for clarity.

halide cleavage and the formation of a cationic metal center, as also observed in the shorter Zn–C^{carbene} bond lengths in the SCXRD. The ^{19}F-NMR spectra of **6–8** and **10** show three distinct resonances at approximately −133, −163.7, and −167.7 ppm, in a 2 : 1 : 2 ratio, which are assigned to the $[B(C_6F_5)_4]^-$ counter-ion. Compounds **6–8** and **10** in DCM solutions were further characterized by ESI-MS, which showed two distinct peaks: one corresponding to M^{2+} and another to $[M - 3(ZnX_2(cAAC)X)]^+$. Both the NMR and mass spectra clearly indicate that the tetrameric motif is also maintained in solution with no monomerization observed.

To further explore different coordination environments and their influence on the excited-state nature, we attempted halide exchange in $[Zn_2Cl_2(\mu\text{-}Cl)_2(^{Me}cAAC)_2]$ (**1**) with monoanionic bidentate acetylacetonate (acac) or monodentate carbazolate (Cz) ligands. Both ligands are known to be promising donors that form ligand-to-ligand charge transfer (LLCT) states in Cu^I emitters, which have applications in OLEDs and NIR emitters.[11,48–51] The reaction of one equivalent of sodium acetylacetonate or potassium carbazolate with **1** in THF yields complexes **11** and **12** in 50–70% yield (Fig. 2).

The ^{1}H-NMR spectra of **11** and **12** show a 1 : 1 ratio of resonances for the carbene and acac or Cz, confirming the exchange of one halide with the ligand and complexation. In the ^{13}C-NMR spectrum of **11**, the most downfield signal appears at approximately 246.9 ppm for the carbene carbon, along with a downfield signal at 192.4 ppm for the carbonyl carbon of acac. We also note additional resonances at 3.58 ppm and 1.77 ppm in the ^{1}H-NMR spectrum of **12**, corresponding to a free THF molecule.

Recrystallization of complex **11** by gas-phase diffusion of pentane over a saturated THF solution yields colourless, block-shaped crystals, which were further characterized by X-ray diffraction. Complex **11** crystallizes in the monoclinic $P2_1/n$ space group and adopts a tetrahedral zinc(II) geometry, coordinating one chloride ion in the coordination sphere (Fig. 3). The Zn–Cl and Zn–C^{carbene} bond lengths in **11** of 2.2503(6) and 2.050(1) Å, respectively, are similar to those in the parent $[Zn_2Cl_2(\mu\text{-}Cl)_2(^{Me}cAAC)_2]$,[43] while the Zn–O bond length (1.998 (1) Å) is consistent with known compounds featuring Zn–O bonds.

Recrystallization of complex **12** from a THF/pentane mixture yields light yellow, block-shaped crystals. These crystals are found to be coordinated to one molecule of THF, achieving tetrahedral geometry around the zinc(II) centre, along with a carbazolate ligand and a terminal chloride ion (Fig. 3). Complex **12** crystallizes in the triclinic $P\bar{1}$ space group, with Zn–Cl and Zn–C^{carbene} bond lengths of 2.2375(6) and 2.046(2) Å, respectively. The Zn–N bond length in **12** is approximately 1.975(1) Å, which is consistent with the Zn–N bond length in other zinc-carbazolate complexes, such as [ZnCl(Cz)(ITr)] (~1.94 Å).[42] The THF coordination in **12** in solution is supported by the presence of a free THF peak in the ^{1}H-NMR spectrum, which may result from ligand exchange with THF-d_8.

Complexes **6–12** are extremely sensitive to oxygen and moisture, both in the solid and solution states. They gradually decompose to form protonated carbene salts in the presence of moisture. This sensitivity is also observed in the parent halides **1–5**, which we attribute to the absence of bulkier groups that would protect the Zn–carbene bond. As a result, further handling and photophysical measurements of complexes **6–12** must be conducted under an inert atmosphere.

UV/Vis absorption studies

Complexes **3–5** undergo photo-decomposition under continuous irradiation with 300 nm light as also observed for **1** and **2**,[43] so further photophysical measurements were not continued for them (Fig. S31). The absorption spectra of the tetrameric compounds **6–8** and **10** in dichloromethane predominantly exhibit a high-energy band (Fig. 4, top), which is consistent with their colourless nature. This band has a broad feature with a maximum absorption at λ_{max} = 260 nm with an extinction coefficient of *ca.* 20 000 M^{-1} cm^{-1}. This absorption is primarily attributed to a mixture of LC$_{\pi-\pi^*}$ transitions, with minor contributions from halide-to-carbene (XLCT) transitions, as suggested by TD-DFT calculations (Fig. 4, bottom). Additionally, we observe some tailing of this band in the

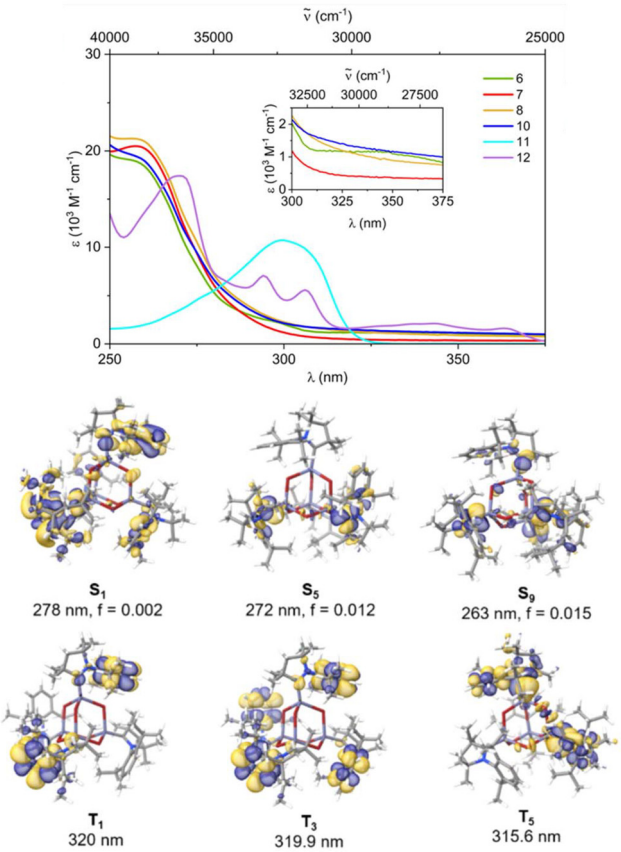

Fig. 4 Top: UV-vis absorption spectra of **6–8** and **10–11** in CH_2Cl_2, and of **12** in THF at room temperature. Bottom: Electron density differences of selected vertical $S_0 \rightarrow S_n$ transitions relevant for the experimental absorption spectra of **7** in DCM and of selected triplet excited states calculated at the D3(BJ)-PBE0/ZORA/def2-SVP level of theory. Loss of electron density is indicated in blue and gain in yellow.

lower-energy region. TD-DFT analysis indicates that this region is associated with spin-forbidden triplet states. However, due to the insignificant SOC of the zinc(II) ion, the observed high extinction coefficients of up to 1000 M^{-1} cm^{-1} must be the result of the structural fluxionality of the molecule in solution in combination with SOC mediated by the halides, leading to an increased transition probability for ISC in this region.

Complex [ZnCl(acac)(^{Me}cAAC)] (**11**) also exhibits only high-energy absorption (Fig. 4, top), as expected from its colourless appearance. The spectral shape of **11** is somewhat similar to that of [Cu(acac)(^{Me}cAAC)],[48] except for the visible energy bands that arise mainly from Cu/acac → π^*_{Dipp} (cAAC) charge transfer (MLCT and LLCT) transitions in the latter complex. The broad higher-energy absorption band of **11** with λ_{max} = 300 nm and ε = 10 000 M^{-1} cm^{-1} possibly results from a mixture of XLCT and LLCT transitions (acac → cAAC) as well as some LE states. The hypsochromic shift of the absorption band observed in comparison to the copper(I) complex is likely due to the absence of the MLCT contribution which contributes to the absorption of visible light.

UV-Vis absorption of [ZnCl(Cz)(THF)(^{Me}cAAC)] (**12**) (Fig. 4) was measured in THF to retain its THF-coordinated structure, showing the lowest energy band at λ_{max} = 360 nm with ε = 1600 M^{-1} cm^{-1} along with an overlapping band at 345 nm (ε = 2100 M^{-1} cm^{-1}). These low energy bands are assigned to originate from an admixture of LLCT transition from the Cz to the ^{Me}cAAC acceptor unit and XLCT. A vibrationally resolved band at 295–305 nm (ε = 5 600–7000 M^{-1} cm^{-1}) is observed, which we attribute to $LC_{\pi-\pi^*}$ transitions of the Cz ligand. Additionally, higher energy bands (λ < 280 nm) are attributed to π–π* transitions of the cAAC ligands.

Luminescence properties

When irradiated with 265 nm light in DCM solution at room temperature, tetramers **6** and **7** exhibit structureless high energy emission with a maximum at *ca.* 375 nm, while [Zn_4(μ-Cl)$_6$(^{Cy}cAAC)$_4$] (**10**) shows well-resolved emission between 375 and 425 nm along with a weak and broad low energy band between 450–680 nm (Fig. 5). Since no significant change was observed when switching from chloride to bromide, we conclude that the high-energy emission is purely carbene-centred. We propose that different conformers present in the solution state contribute to significant broadening of the bands observed for compounds **6** and **7**. In contrast, the higher rigidity imparted by the steric constraints of the cyclohexyl group in **10** may result in a larger energy barrier between these conformations, leading to the more resolved emission observed in solution. The excitation-dependent emission spectra of [Zn_4(μ-Br)$_6$(^{Me}cAAC)$_4$] (**7**) produce structurally resolved high-energy emission, with a slight hypsochromic shift in the emission maximum (Fig. 5, bottom right). As the excitation energy decreases, a new lower-energy emission band becomes more prominent similar to that observed for **10**, indicating a shift in the relative population of excited states.

In the solid state, upon excitation with 265 nm light, compounds **6–8** and **10** exhibit broad, structureless emission with

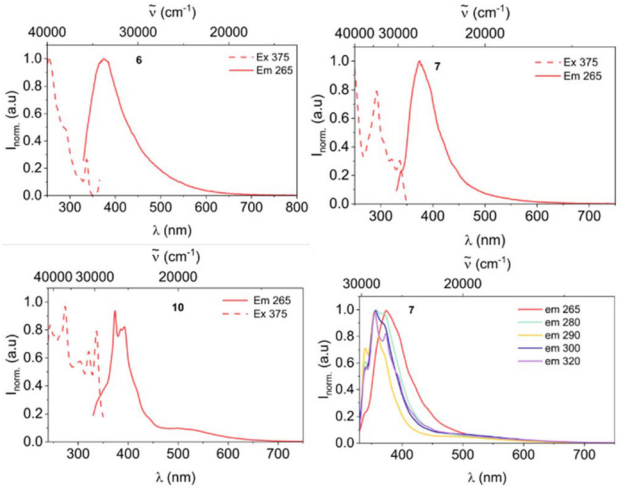

Fig. 5 Emission (λ_{ex} = 265 nm) and excitation (λ_{em} = 375 nm) spectra of **6**, **7** (top) and **10** (bottom left) in DCM at 297 K, and excitation wavelength-dependent emission spectra of **7** in DCM at 297 K (bottom right).

a slight bathochromic shift in comparison to solution state, peaking around λ_{max} = 385–390 nm (Fig. 6 and Table 1). Under continuous photo-irradiation, the luminescence intensity decreases, indicating photo-chemical transformations occurring in these compounds. The changes are most pronounced in [Zn_4(μ-Cl)$_6$(^{Me}cAAC)$_4$] (**6**) with a new low-energy emission band at 497 nm appearing (Fig. 7, left), while **7**, **8** and **10** show a similar decrease in emission intensity, but without the formation of additional bands within the 10 minutes timescale (Fig. S32).

Importantly, the presence of an isosbestic point for **6** suggests that the spectral changes are not due to decomposition, but instead result from a specific conformational change in the excited state, leading to the formation of a single, new species that emits from the low energy state. A similar phenomenon has been observed in [Zn_2Cl_2(μ-Cl)$_2$(^{Me}cAAC)$_2$], where the intensity of a high-energy band at λ_{max} = 360 nm (associated with the ^{3}XLCT transition) diminishes, while the intensity of a broad low-energy band at λ_{max} = 451 nm (attributable to a $^3LE_{cAAC}$ transition) increases.[43] This transformation was linked to asymmetric distortion of the cAAC ligand along the Zn–carbene bond, along with other unidentified processes. However, due to the higher rigidity of the tetrameric clusters **6–8** and **10**, the rate of photo-transformation is comparatively slower than in the previous dimer, where photo-chemical changes occur within just a few minutes.

Since the 265 nm excitation directly interacts with the Zn–carbene bond as indicated by TD-DFT calculations (Fig. S33), we propose that photo-irradiation causes compound **6** to undergo a geometry change involving that particular bond. The rate of this photo-transformation (**6** > **8** ≫ **10** > **7**) is influenced by the structural rigidity of the complexes (Fig. 7, bottom left), which varies depending on the substituents on the cAAC ligand. The much slower rate of decomposition in

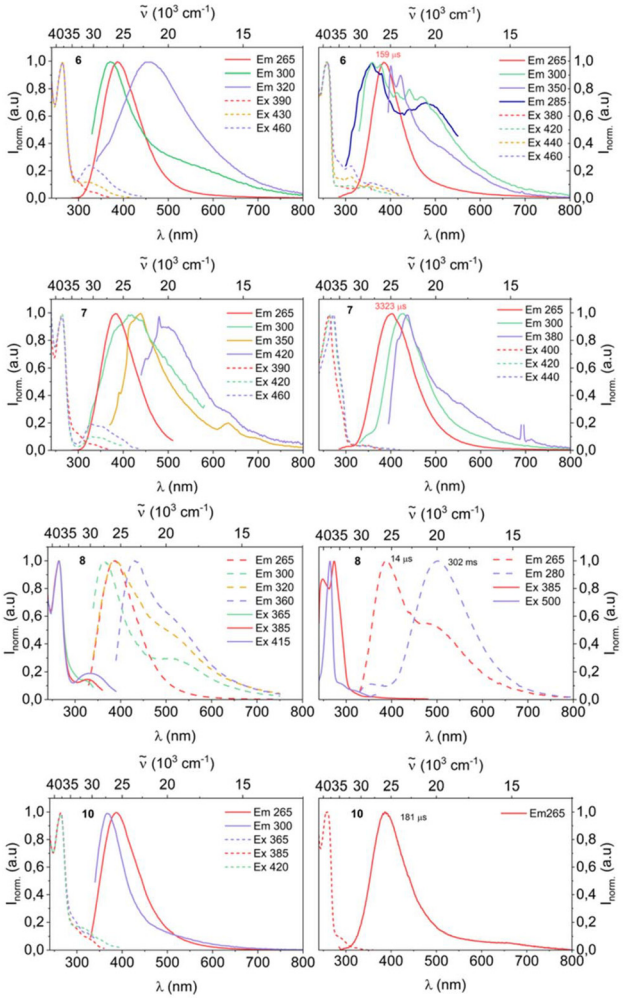

Fig. 6 Emission and excitation spectra of **6–8** and **10** in the solid state at 297 K (left) and 77 K (right).

Table 1 Selected photophysical data for **6–8** and **10–12** in the solid state

Cpd.	λ_{ex} (nm)	T (K)	λ_{em} (nm)	τ (μs)	Φ
6	265	297	386	—	<0.01
		77	385	159	
7	265	297	390	—	<0.01
		77	400	3323	
8	265	297	385	—	<0.01
		77	385	14	
			500	302	
10	265	297	385	—	<0.01
		77	385	181	
11	320	297	422, 484, 507	—	0.03
		77	422, 480, 510	42×10^3	0.05
12	370	297	590	—	<0.01
		77	580	41	0.09

$[Zn_4(\mu\text{-Br})_6(^{Me}cAAC)_4]$ (**7**) in comparison to the chloride analogue **6**, or the more bulky carbene bearing clusters **8** and **10**, is somewhat unexpected, as one might anticipate higher photo-conversion due to the presence of smaller methyl substituents and the weaker Zn–Br bond strength. This assumption holds true if the Zn–X bonds were involved in the conformational change. However, as the change mostly occurs at the carbene and/or Zn–$C^{carbene}$ bond, thus the halides may just influence the ISC pathways, which may alter the relative populations of excited states. Therefore, while the halide influence appears to play a role, the exact mechanism remains inconclusive and any further hypothesis is highly speculative as the available analytical methods to characterize the excited state kinetics further are not applicable to the solid state samples. However, the finding that the low energy band does not form when **6** is being excited at 77 K is in line with these conclusions (Fig. 7, bottom right).

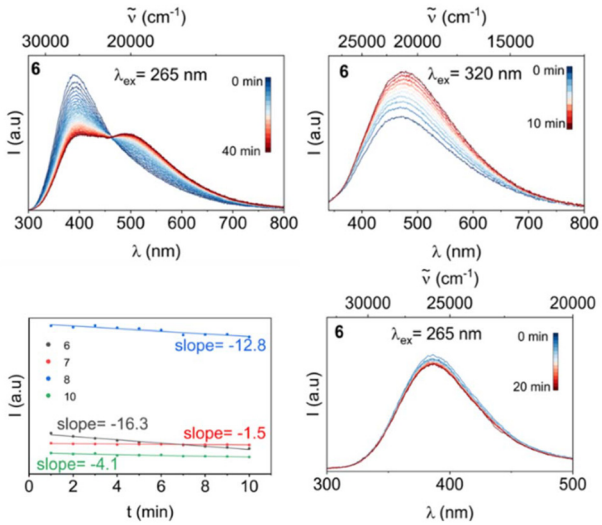

Fig. 7 Top: Temporal evolution of the emission spectrum of **6** in solid state at 297 K (λ_{ex} = 265 nm, left; λ_{ex} = 320 nm, right). Bottom: Temporal evolution of the emission intensity at λ_{max} = 385 nm of **6–8** and **10** in the solid state at 297 K (left), and of the emission spectrum of **6** in the solid state at 77 K (right).

Surprisingly, when excited with lower-energy light (λ_{ex} > 265 nm), compounds **6–8** exhibit different additional low-energy emission bands, a change that is much less pronounced for $[Zn_4(\mu\text{-Cl})_6(^{Cy}cAAC)_4]$ (**10**) (Fig. 6). This suggests that structural rigidity plays an important role in determining the relative population of different states involved in the emission of the tetrameric clusters *via* excited-state geometry changes, giving rise to dual phosphorescence behaviour. The excitation spectra for the low-energy emission bands (λ_{max} > 385 nm) also significantly shift, intensifying in the lower energy region (300–390 nm). The time-dependent emission spectra, excited at 320 nm (corresponding to the triplet state energy region as determined by TD-DFT), reveal a continuous increase in the intensity of the lower-energy band at 490 nm for compound **6** (Fig. 7, top right). This behaviour suggests that direct excitation into the triplet state triggers an immediate conformational change, occurring more rapidly than the conformational transition pathway accessed through higher-lying excited states. These newly formed conformers appear to

persist, at least partially, in the ground state, thereby contributing to increased absorptivity in the macroscopic sample and a corresponding growth in emission intensity. However, the low intensity of the emission bands prevents accurate determination of the emission lifetimes, making it difficult to ascertain the nature of the emissions at room temperature.

To resolve the emission mechanism and prevent photochemical transformation, further photophysical studies were carried out at 77 K in the solid state. A slight redshift to 400 nm is observed for compound **7**, while emissions for compounds **6** and **10** remain unchanged regardless of temperature under 265 nm irradiation (Fig. 6) and a new emission band at 500 nm is observed for compound **8** alongside the major 385 nm band. Time-resolved measurements reveal luminescence lifetimes in the micro-to-millisecond regime for the 385 nm emission in compounds **6–8** and **10**, with compound **8** showing a comparatively short lifetime of 14 μs at the emission maximum, which indicates triplet states being involved in the emission (Table 1).

We attribute the observed luminescence to carbene-centred triplet states localized at the aromatic *N*-substituent, with some minor XLCT contribution. The significant overlap of emission and excitation spectra, as mentioned before, indicates that the low-energy excitation band (320–390 nm) is also triplet in nature. TD-DFT calculations for compound **7** show that several triplet states (λ = 320 nm, 319.9 nm, 315.6 nm) exist in this region (Fig. 4, bottom). While these states are mainly carbene-based, different contributions from the carbene and the halides lead to nearly degenerate triplet states. These states are also vibrationally resolved in the 77 K excitation spectra.

When excited with lower-energy light (*e.g.*, 300 or 320 nm), different triplet excited states can be populated depending on the excitation wavelength, the energy gap between these states, and the activation barrier for transitions between them, all of which are influenced by the molecular structure. The system can either be directly excited to a low-energy triplet state or repopulate from the initially populated high-energy state, which involves a geometry change upon excitation (Fig. 8). The radiative rates k_r and k_r' also play a crucial role in determining the possible emission outcomes. With high-energy excitations, where $k_r > k_r'$, the emission predominantly originates from the high-energy state. Thus, the equilibrium between high- and low-energy states leads to different emission behaviours for compounds **6–8** and **10** under varying excitation energies. This assumption is further supported by the different emission lifetimes observed at 77 K. For **6**, under 265 nm irradiation, only one emission at 385 nm is observed, corresponding to a long-lived triplet state with a lifetime of 159 μs, with no low-energy emission detected. This suggests a very fast equilibrium between the two conformers, with the emission predominantly coming from the higher-energy state. In contrast, for compound **10**, the rigid structure prevents significant geometry changes upon excitation, resulting in a major 385 nm emission with a similar lifetime. For compound **8**, two emissions are observed upon 265 nm excitation, the primary 385 nm emission is relatively short-lived, as it decays preferentially to a low-energy state, resulting in emission at 500 nm. The lifetime of this low-energy state is recorded at 302 ms, confirming its triplet origin. However, the relatively long lifetime observed for compound **8** cannot be fully explained by this mechanism, indicating that additional processes may be involved. The observed photophysical behaviour of the tetramers suggests that high-energy excitation leads to emission primarily from the high-energy state, likely due to a strong Franck–Condon overlap of the transition, while emission from the low-energy excited state is suppressed or 'trapped'. On the other hand, low-energy excitation promotes direct triplet excitations and repopulation of the lower-energy triplet from higher-lying triplet states. This process is dependent on the structural properties of the molecule, which influence the energy gap and intersystem crossing rates. This rigidity-dependent excited state behaviour is driven by the equilibrium between the two excited states, which is regulated by geometry changes in the excited state, highlighting the importance of molecular structure in determining the emission profile.

Upon irradiation with 320 nm light, [ZnCl(acac)(^{Me}cAAC)] (**11**) shows two different emission maxima at 420 nm and 480 nm along with a shoulder at 507 nm (Fig. 9). We hypothesize that the emission of compound **11** arises simultaneously from LE, LLCT and XCT states. Although the complex does not

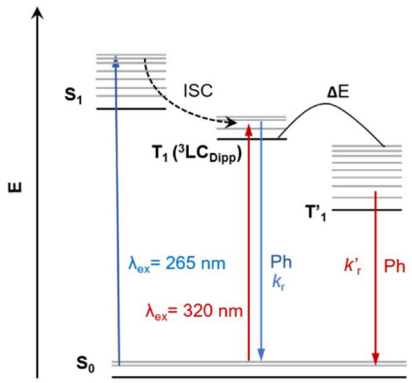

Fig. 8 Schematic diagram of the emission mechanism of tetrameric **6–8** and **10**.

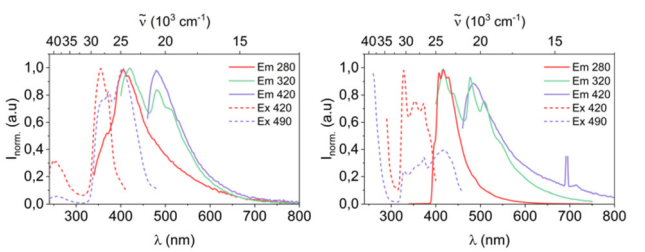

Fig. 9 Emission and excitation spectra of **11** in the solid state at 297 K (left) and 77 K (right).

exhibit any absorption beyond 325 nm, consistent with its colourless appearance, the excitation spectra of compound **11** at 420 nm reveal an intense low-energy band between 330 and 400 nm. This band is attributed to direct triplet absorption, likely enabled by the effectively infinite concentration of molecules in the solid state, which allows otherwise forbidden transitions to become observable.

Upon cooling to 77 K, a similar but structurally resolved emission spectrum is observed under 320 nm excitation. The photoluminescence lifetime at 480 nm emission maximum is 42.1 ms, with a quantum yield of 0.05, leading to a radiative rate constant of 1.2 s^{-1}. This supports the involvement of triplet states in the emission process and thus phosphorescence. Excitation with 280 nm light leads to only emission at high energy band at 420 nm at 297 K, which shows vibrational progression at 77 K, indicating involvement of LE states. When irradiated with 420 nm, structureless, broad emission at λ_{max} = 485 nm is observed at both temperatures. Presumably, this emission is of CT nature, which is exclusively getting populated with low energy excitation.

When excited with 370 nm light in the solid state, [ZnCl(Cz)(THF)(^{Me}cAAC)] (**12**) exhibits weak yellow photoluminescence with broad emission peaking at λ_{max} = 590 nm (Fig. 10). The broad nature of this emission band suggests a charge transfer (CT) character, likely a LLCT transition from the Cz to the carbene moiety. Similar broad LLCT emissions have been documented in the literature for complexes such as [Zn_2(bdt)$_2$(MecAAC)$_2$] and [Zn(bdt)(MenthcAAC)], both of which display broad, featureless yellow-orange emission, with thermally activated delayed fluorescence (TADF) as the primary radiative pathway.[15,44] To further investigate the emission mechanism, compound **12** was cooled to 77 K, where it exhibited a slight hypsochromic shift in the emission, likely due to rigidification at lower temperature. This shift was accompanied by an enhanced emission lifetime of 41 μs, leading to a radiative rate constant of 2.1 × 10^3 s^{-1}, indicative of triplet-state emission. The 77 K emission spectrum also revealed a small shoulder at 450 nm, which may arise from a ^{3}Cz state, a feature also observed in the emission of [Cu(Cz)(^{Menth}cAAC)].[11]

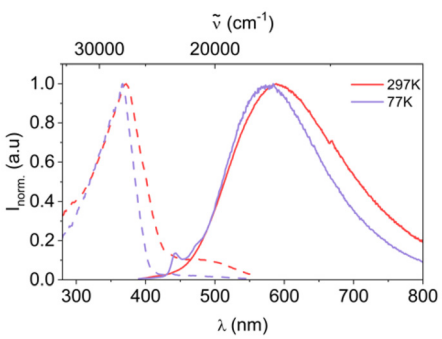

Fig. 10 Emission and excitation spectra of **12** in the solid state at 297 K and 77 K.

Conclusion

We have synthesized a series of adamantane-like tetrameric cationic zinc compounds based on cAAC with halides as bridging ligands (**6–10**). Additionally, we have prepared tetrahedral zinc(II) complexes with acac or Cz ligands, with one chloride terminally attached. Halide abstraction or exchange from the parent halide dimer leads to the formation of entirely new zinc (II) structural motifs. All of the synthesized complexes exhibit phosphorescence as their emission pathway, though the origin of the emission varies with the structural motif. The clusters **6–8** and **10** show emission in the high-energy range most likely from ^{3}LE states and, depending on the substituents, they appear to undergo conformation change to populate lower energy triplet states and emit from there. The experimental data suggest that the observed rigidity-dependent dual phosphorescence behaviour arises from an equilibrium between the two excited states, governed by geometry changes in the excited state. While acac coordination (**11**) results in very structured emission in the high-energy range, attributed to a localized excited state, the coordination of carbazolate leads to broad LLCT emission in the yellow region of the spectrum. Although these compounds are weakly emissive in the solid state, which limits their potential applications, they offer valuable insights into the photophysical properties of zinc(II) compounds, particularly in relation to triplet emission and the rare observation of phosphorescence emission in zinc(II) complexes.

Conflicts of interest

There are no conflicts to declare.

Data availability

Supplementary information (SI): synthesis details, characterisation data for compounds including NMR spectroscopy, mass spectrometry, single crystal X-ray diffraction data, theoretical studies, and photophysical data. See DOI: https://doi.org/10.1039/d6dt00177g.

CCDC 2404735–2404742 contain the supplementary crystallographic data for this paper.[52a–h]

Acknowledgements

This work was supported by Deutsche Forschungsgemeinschaft [DFG, Priority Program SPP 2102 "Light-controlled reactivity of metal complexes" (MA 1051/18-1 and STE 1834/7-1)]. We are also grateful to the DFG for funding of major research equipment (INST 212/430-1 FUGG and INST 212/455-1 FUGG). A. B. is grateful to Alexander von Humboldt Foundation for a Research Fellowship grant for Postdoctoral Research.

References

1 M. Soleilhavoup and G. Bertrand, *Acc. Chem. Res.*, 2015, **48**, 256–266.
2 N. V. Tzouras, E. A. Martynova, X. Y. Ma, T. Scattolin, B. Hupp, H. Busen, M. Saab, Z. Y. Zhang, L. Falivene, G. Pisanò, K. Van Hecke, L. Cavallo, C. S. J. Cazin, A. Steffen and S. P. Nolan, *Chem. – Eur. J.*, 2021, **27**, 11904–11911.
3 M. Melaimi, R. Jazzar, M. Soleilhavoup and G. Bertrand, *Angew. Chem., Int. Ed.*, 2017, **56**, 10046–10068.
4 V. Lavallo, Y. Canac, C. Präsang, B. Donnadieu and G. Bertrand, *Angew. Chem., Int. Ed.*, 2005, **44**, 5705–5709.
5 J. Chu, D. Munz, R. Jazzar, M. Melaimi and G. Bertrand, *J. Am. Chem. Soc.*, 2016, **138**, 7884–7887.
6 U. S. D. Paul and U. Radius, *Eur. J. Inorg. Chem.*, 2017, 3362–3375.
7 R. Jazzar, M. Soleilhavoup and G. Bertrand, *Chem. Rev.*, 2020, **120**, 4141–4168.
8 P. Bellotti, M. Koy, M. N. Hopkinson and F. Glorius, *Nat. Rev. Chem.*, 2021, **5**, 711–725.
9 S. K. Kushvaha, A. Mishra, H. Roesky and K. C. Mondal, *Chem. – Asian J.*, 2022, **17**, e202101301.
10 M. Gernert, U. Müller, M. Haehnel, J. Pflaum and A. Steffen, *Chem. – Eur. J.*, 2017, **23**, 2206–2216.
11 R. Hamze, J. L. Peltier, D. Sylvinson, M. Jung, J. Cardenas, R. Haiges, M. Soleilhavoup, R. Jazzar, P. I. Djurovich, G. Bertrand and M. E. Thompson, *Science*, 2019, **363**, 601–606.
12 T. Y. Li, S. J. Zheng, P. I. Djurovich and M. E. Thompson, *Chem. Rev.*, 2024, **124**, 4332–4392.
13 Y. Q. Ding, R. Goddard and K. R. Pörschke, *Organometallics*, 2005, **24**, 439–445.
14 L. Q. Jin, D. S. Weinberger, M. Melaimi, C. E. Moore, A. L. Rheingold and G. Bertrand, *Angew. Chem., Int. Ed.*, 2014, **53**, 9059–9063.
15 M. Mitra, O. Mrózek, M. Putscher, J. Guhl, B. Hupp, A. Belyaev, C. M. Marian and A. Steffen, *Angew. Chem., Int. Ed.*, 2024, **63**, e202316300.
16 J. Hossain, R. Akhtar and S. Khan, *Polyhedron*, 2021, **201**, 115151.
17 A. Ruduss, A. Jece, K. A. Stucere, K.-W. Chen, B. Turovska, S. Belyakov, A. Vembris, C.-H. Chang and K. Traskovskis, *J. Mater. Chem. C*, 2024, **12**, 2968–2980.
18 A. Farokhi, S. Lipinski, L. M. Cavinato, H. Shahroosvand, B. Pashaei, S. Karimi, S. Bellani, F. Bonaccorso and R. D. Costa, *Chem. Soc. Rev.*, 2024, **54**, 266–340.
19 G. Morselli, C. Reber and O. S. Wenger, *J. Am. Chem. Soc.*, 2025, **147**, 11608–11624.
20 S. Bestgen, C. Schoo, B. L. Neumeier, T. J. Feuerstein, C. Zovko, R. Köppe, C. Feldmann and P. W. Roesky, *Angew. Chem., Int. Ed.*, 2018, **57**, 14265–14269.
21 K. D. Oyler, F. J. Coughlin and S. Bernhard, *J. Am. Chem. Soc.*, 2007, **129**, 210–217.
22 J. Kuhnt, M. Mitra, S. Maity, B. Hupp, C. M. Marian and A. Steffen, *J. Phys. Chem. Lett.*, 2024, **15**, 6409–6414.
23 I. Y. Chan, W. G. van Dorp, T. J. Schaafsma and J. H. van der Waals, *Mol. Phys.*, 1971, **22**, 753–760.
24 A. Harriman, *J. Chem. Soc., Faraday Trans.*, 1980, **76**, 1978–1985.
25 P. J. Gronlund, J. A. Burt and W. F. Wacholtz, *Inorg. Chim. Acta*, 1995, **234**, 13–18.
26 E. Kimura and T. Koike, *Chem. Soc. Rev.*, 1998, **27**, 179–184.
27 V. Yam and K. K. Lo, *Chem. Soc. Rev.*, 1999, **28**, 323–334.
28 A. Gusev, E. Braga, E. Zamnius, M. Kiskin, M. Kryukova, A. Baryshnikova, B. Minaev, G. Baryshnikov, H. Ågren and W. Linert, *RSC Adv.*, 2019, **9**, 22143–22152.
29 R. Diana and B. Panunzi, *Molecules*, 2020, **25**, 4984.
30 H. Deng, T. Wang, Y. Chen, K. Dou, X. Liu, C. Zhao, H. Zhan, C. Yang, C. Qin and Y. Cheng, *J. Phys. Chem. Lett.*, 2024, **15**, 7003–7010.
31 S. A. Elgadi, S. Mikulin and Z. Hudson, *Adv. Opt. Mater.*, 2025, **13**, 2500683.
32 D. A. Shariaty, P. I. Djurovich and M. E. Thompson, *J. Am. Chem. Soc.*, 2025, **147**, 29065–29078.
33 D. A. Shariaty, J. Schaab, E. McClure, T. Nattikalungal, P. I. Djurovich, S. Bradforth and M. E. Thompson, *Inorg. Chem.*, 2025, **64**, 1228–1240.
34 Y. Sakai, Y. Sagara, H. Nomura, N. Nakamura, Y. Suzuki, H. Miyazaki and C. Adachi, *Chem. Commun.*, 2015, **51**, 3181–3184.
35 G. A. Crosby, R. G. Highland and K. A. Truesdell, *Coord. Chem. Rev.*, 1985, **64**, 41–52.
36 R. G. Highland and G. A. Crosby, *Chem. Phys. Lett.*, 1985, **119**, 454–458.
37 J. A. Burt and G. A. Crosby, *Chem. Phys. Lett.*, 1994, **220**, 493–496.
38 V. W. W. Yam, Y. L. Pui and K. K. Cheung, *Inorg. Chim. Acta*, 2002, **335**, 77–84.
39 V. W. W. Yam, Y. L. Pui, K. K. Cheung and N. Y. Zhu, *New J. Chem.*, 2002, **26**, 536–542.
40 T. W. Ngan, C. C. Ko, N. Zhu and V. W. Yam, *Inorg. Chem.*, 2007, **46**, 1144–1152.
41 N. Lüdtke, J. Kuhnt, T. Heil, A. Steffen and C. M. Marian, *ChemPhotoChem*, 2023, **7**, e202200142.
42 S. Koop, O. Mrózek, L. Janiak, A. Belyaev, M. Putscher, C. M. Marian and A. Steffen, *Inorg. Chem.*, 2023, **63**, 891–901.
43 O. Mrózek, M. Gernert, A. Belyaev, M. Mitra, L. Janiak, C. M. Marian and A. Steffen, *Chem. – Eur. J.*, 2022, **28**, e202201114.
44 O. Mrózek, M. Mitra, B. Hupp, A. Belyaev, N. Lüdtke, D. Wagner, C. Wang, O. S. Wenger, C. M. Marian and A. Steffen, *Chem. – Eur. J.*, 2023, **29**, e202203980.
45 J. B. Lambert, S. H. Zhang, C. L. Stern and J. C. Huffman, *Science*, 1993, **260**, 1917–1918.
46 J. B. Lambert, S. Z. Zhang and S. M. Ciro, *Organometallics*, 1994, **13**, 2430–2443.
47 N. Rinn, I. Rojas-León, B. Peerless, S. Gowrisankar, F. Ziese, N. W. Rosemann, W. C. Pilgrim, S. Sanna, P. R. Schreiner and S. Dehnen, *Chem. Sci.*, 2024, **15**, 9438–9509.

48 A. M. T. Muthig, M. Krumrein, J. Wieland, M. Gernert, F. Kerner, J. Pflaum and A. Steffen, *Inorg. Chem.*, 2022, **61**, 14833–14844.
49 S. Y. Shi, M. C. Jung, C. C. A. Tadle, M. R. D. Sylvinson, P. I. Djurovich, S. R. Forrest and M. E. Thompson, *J. Am. Chem. Soc.*, 2019, **141**, 3576–3588.
50 A. M. T. Muthig, O. Mrózek, T. Ferschke, M. Rödel, B. Ewald, J. Kuhnt, C. Lenczyk, J. Pflaum and A. Steffen, *J. Am. Chem. Soc.*, 2023, **145**, 4438–4449.
51 M. Gernert, L. Balles-Wolf, F. Kerner, U. Müller, A. Schmiedel, M. Holzapfel, C. M. Marian, J. Pflaum, C. Lambert and A. Steffen, *J. Am. Chem. Soc.*, 2020, **142**, 8897–8909.
52 (*a*) CCDC 2404735: Experimental Crystal Structure Determination, 2026, DOI: 10.5517/ccdc.csd.cc2lqb3s; (*b*) CCDC 2404736: Experimental Crystal Structure Determination, 2026, DOI: 10.5517/ccdc.csd.cc2lqb4t; (*c*) CCDC 2404737: Experimental Crystal Structure Determination, 2026, DOI: 10.5517/ccdc.csd.cc2lqb5v; (*d*) CCDC 2404738: Experimental Crystal Structure Determination, 2026, DOI: 10.5517/ccdc.csd.cc2lqb6w; (*e*) CCDC 2404739: Experimental Crystal Structure Determination, 2026, DOI: 10.5517/ccdc.csd.cc2lqb7x; (*f*) CCDC 2404740: Experimental Crystal Structure Determination, 2026, DOI: 10.5517/ccdc.csd.cc2lqb8y; (*g*) CCDC 2404741: Experimental Crystal Structure Determination, 2026, DOI: 10.5517/ccdc.csd.cc2lqb9z; (*h*) CCDC 2404742: Experimental Crystal Structure Determination, 2026, DOI: 10.5517/ccdc.csd.cc2lqbb0.